

REPORTS

LOW-DENSITY MATERIALS

Strong, lightweight, and recoverable three-dimensional ceramic nanolattices

Lucas R. Meza,¹ Satyajit Das,^{1*} Julia R. Greer^{1,2†}

Ceramics have some of the highest strength- and stiffness-to-weight ratios of any material but are suboptimal for use as structural materials because of their brittleness and sensitivity to flaws. We demonstrate the creation of structural metamaterials composed of nanoscale ceramics that are simultaneously ultralight, strong, and energy-absorbing and can recover their original shape after compressions in excess of 50% strain. Hollow-tube alumina nanolattices were fabricated using two-photon lithography, atomic layer deposition, and oxygen plasma etching. Structures were made with wall thicknesses of 5 to 60 nanometers and densities of 6.3 to 258 kilograms per cubic meter. Compression experiments revealed that optimizing the wall thickness-to-radius ratio of the tubes can suppress brittle fracture in the constituent solid in favor of elastic shell buckling, resulting in ductile-like deformation and recoverability.

The ability to decouple properties such as strength and stiffness from density requires the use of advanced processing techniques combined with materials optimized for superior mechanical performance per unit weight. Many monolithic materials with high strength-to-weight (σ_{ys}/ρ) and stiffness-to-weight (E/ρ) ratios—such as technical ceramics, diamond, and metallic glasses—have excellent potential for use as strong and lightweight structural materials but are suboptimal because of their low toughness and brittle, flaw-sensitive nature. Some of these materials exhibit size effects in mechanical properties when reduced to nanoscale dimensions, such as improved strength (1, 2), flaw tolerance (3), and enhanced ductility (4, 5). Architected lightweight structures made from high-strength nanoceramics (1, 6, 7) and nanoceramic composites (8) have been reported to have enhanced strengths and stiffnesses, but they still suffer from brittle, catastrophic failure. Efforts to toughen fully dense brittle materials have focused primarily on using microstructural features to impede crack motion (9–11) and on forming composites (12, 13), but these approaches have seen limited success in lightweight structures. Many natural hard materials such as sea sponge skeletons (14) and diatom shells (15) are simultaneously stiff, tough, and lightweight, a combination of properties that is thought to be attained by a hierarchical design of components within their bodies (16).

Lightweight structures that are both strong and tough may be engineered by utilizing such hierarchical design principles. The yield strength and stiffness of cellular structures scale as $\sigma_y \propto \sigma_{ys} \bar{\rho}^n$ and $E \propto E_s \bar{\rho}^m$, where $\bar{\rho}$ is the relative density, σ_{ys} and E_s are the yield strength and stiffness of the parent solid, and exponents n and m are

functions of the architecture (17). Cellular geometries that typically lead to the highest strength are stretching-dominated, meaning that they have no intrinsic mechanisms that allow for bending of the individual truss members (18, 19). The yield strength and stiffness of an ideal stretching-dominated structure scale linearly with relative density as $\sigma_y \sim \bar{\rho}$ and $E \sim \bar{\rho}$ (20). This is in contrast to architectures that are either periodic and bending-dominated, whose modulus scales as $E \sim \bar{\rho}^2$, or stochastic, with $E \sim \bar{\rho}^3$ scaling (21).

We created a strong, stiff, and energy-absorbing hollow-tube nanolattice with an octet-truss geometry (Fig. 1) that consists solely of a brittle ceramic, aluminum oxide (alumina), and exhibits nearly full recoverability after compressions in excess of 50% strain. Nanomechanical experiments reveal that the Young's modulus of our nanolattices scales with relative density as $E \sim \bar{\rho}^{1.61}$, and failure strength scales as $\sigma_f \sim \bar{\rho}^{1.70}$, which differ from the analytical scaling for both stretching- and bending-dominated structures because of the hollow tubes and nodes.

Creation of ceramic nanolattices begins with the design and writing of a three-dimensional (3D) polymer scaffold using two-photon lithography direct laser writing. A thin alumina film is then deposited onto the polymer scaffold by atomic layer deposition (ALD), so that it coats the entire surface. The outermost walls of the coated structure are then removed by focused ion beam milling (FIB), and the internal polymer is etched away in O_2 plasma. The resulting 3D freestanding ceramic nanolattice consists of a network of hollow tubes, as shown in Fig. 1. This fabrication

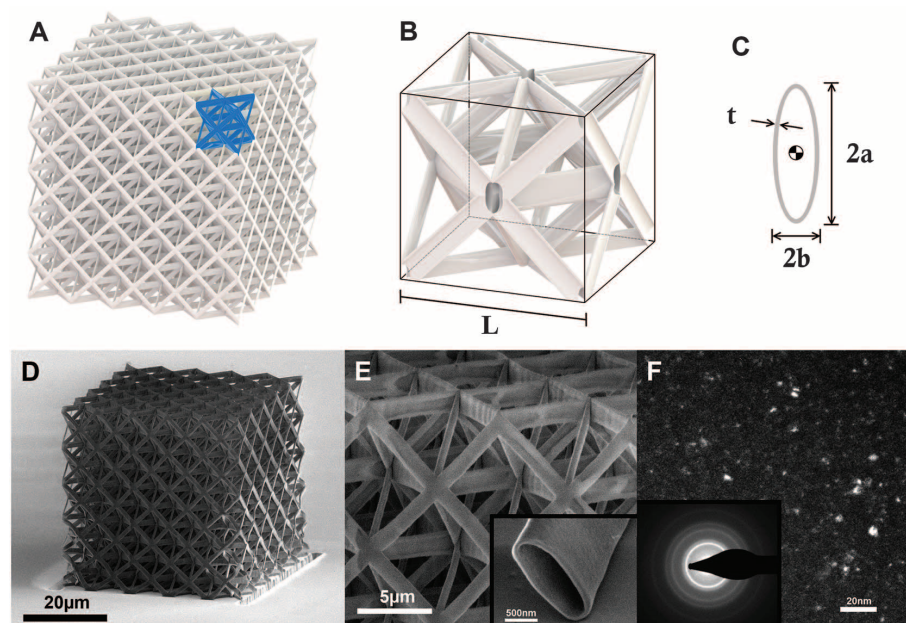


Fig. 1. Architecture, design, and microstructure of alumina nanolattices. (A) CAD image of the octet-truss design used in the study. The blue section represents a single unit cell. (B) Cutaway of hollow octet-truss unit cell. (C) Hollow elliptical cross section of a nanolattice tube. (D) SEM image of alumina octet-truss nanolattice. (E) Zoomed-in section of the alumina octet-truss nanolattice. The inset shows an isolated hollow tube. (F) TEM dark-field image with diffraction grating of the alumina nanolattice tube wall.

¹Division of Engineering and Applied Science, California Institute of Technology, Pasadena, CA, USA. ²Kavli Nanoscience Institute, California Institute of Technology, Pasadena, CA, USA.

*Present address: Department of Engineering, University of Cambridge, Cambridge, UK. †Corresponding author. E-mail: jrgreer@caltech.edu

method enables the creation of 3D structures with numerous geometries (8, 22). Further fabrication details and a schematic of the deposition process can be found in (23) and are shown in fig. S1.

Nanolattices in this work were designed with relative densities spanning $\bar{\rho} = 0.21$ to 8.6%. Using a reported value for the density of ALD alumina, $\rho_s = 2900 \text{ kg/m}^3$ (24), the absolute densities of nanolattices were calculated to be $\rho = 6.1$ to 249 kg/m^3 , which places the lightest ones into the ultralight regime, defined as materials with densities $\leq 10 \text{ kg/m}^3$ (27). This density range is comparable to that of aerogels (25) and other ultralight materials (7, 27). In this work, nanolattices were designed to have tube wall thicknesses t of 5 to 60 nm, tube major axis a of 0.45 to $1.38 \mu\text{m}$, and unit cell widths L of 5 to $15 \mu\text{m}$ (Fig. 1, B and C), spanning length scales that can be controlled across four orders of magnitude. Transmission electron microscopy (TEM) analysis revealed ALD alumina to contain 2- to 10-nm nanocrystalline precipitates intermixed in an amorphous matrix (Fig. 1F). A list of the parameters and relative densities is provided in Table S1.

Monotonic and cyclical uniaxial compression experiments were performed on nanolattices in a G200 XP Nanoindenter (Agilent Technologies). In the first set of experiments, structures were compressed uniaxially to $\sim 50\%$ strain at a rate of 10^{-3} s^{-1} to determine their yield stress and overall deformation characteristics (Figs. 2; 3, A to D; and 4, B and D; and fig. S2A). In the second set of experiments, structures were cyclically loaded and unloaded three times to $\sim 70\%$ of their failure load, and unloading slopes from each cycle were averaged to estimate Young's modulus (Fig. 4, A and C, and fig. S2B). Unloading rather than loading moduli were used to mitigate the possible effects of loading imperfections such as misalignment and partial initial contact (fig. S2B). Additional samples were compressed in an in situ nanomechanical instrument, InSEM (Nanome-

chanics Inc.), to observe local and global deformation characteristics and to investigate the failure modes that occurred during deformation (movies S1 to S3). Stress-strain data and still frames of the in situ compression experiments are shown in Fig. 2.

Two distinct deformation signatures were observed during nanolattice compressions. These are best characterized using the thickness-to-radius ratio of the tubes, t/a , as a figure of merit. Structures with $t/a \geq 0.03$, referred to as thick-walled, demonstrate linear elastic loading followed by catastrophic brittle failure (Fig. 3, A, B, E, and F). An example of a typical deformation and corresponding stress-strain data are shown in Fig. 2, F to J, and movie S3. Compressive stress-strain data for thick-walled structures show large strain bursts, with burst magnitude increasing at greater t/a ; structures with $t/a = 0.032$ have bursts of $\sim 10\%$ strain (Fig. 3B), whereas structures with $t/a = 0.067$ show bursts of $\sim 80\%$ strain (Fig. 3A). This observed increase in burst magnitude is probably driven by greater elastic strain energy stored in thicker-walled structures during deformation. Each strain burst corresponds to a discrete brittle failure event, which leads to permanent damage of the structure (Figs. 2J and 3, E and F). This type of catastrophic failure has been observed in previous experiments on hollow ceramic nanolattices (6) and ceramic composites (8) and is generally typical of ceramic foams (17).

Thin-walled nanolattices, defined as those with $t/a \leq 0.02$, did not exhibit catastrophic failure or discrete strain bursts. Samples in this regime first deformed elastically, where stress increased linearly with strain, followed by a ductile-like, controlled deformation, with stress plateauing after yielding (Fig. 3, C and D). An example of a typical deformation and corresponding stress-strain data are shown in Fig. 2, A to E, and movie S1. As the t/a of the samples decreased, the serrated burst behavior seen in the thick-walled structures was

suppressed, and stress-strain data became smooth (Fig. 3, C and D). After yielding, all ensuing deformation was accommodated through wrinkling and local buckling of the tube walls (Fig. 2, D and E, and movie S1). All thin-walled ceramic nanolattices exhibited notable recovery after deformation, with some recovering up to $\sim 98\%$ of their original height after compression to 50% strain (Figs. 2E and 3H) and others recovering by $\sim 80\%$ after compression to 85% strain (fig. S4). Structures with smaller unit cells demonstrated greater recoverability, each recovering to at least 95% of its original height. Nanolattices with larger unit cells recovered less on average, but all recovered to at least 75% of their original height (fig. S3). SEM images of post-deformed structures revealed localized cracking on and around the nodes (Fig. 3J), implying that the failure of ALD alumina remained brittle and that the observed deformability and recoverability probably emerged from structural effects.

Nanolattices with $0.02 \leq t/a \leq 0.03$ exhibited a combination of the two described deformation signatures. In these samples, both brittle and ductile-like deformation took place; several minor strain bursts were present, and marginal recovery occurred after compression to 50% strain (Fig. 3, C, G, and I, and movie S2). The in situ deformation movie S2 shows that each strain burst correlates with discrete local brittle fracture events in the tubes, and post-yield ductile-like behavior corresponds to buckling and wrinkling of the tube walls. The transition between these two deformation modes is probably driven by an energetic competition between elastic and brittle failure.

Three competing failure mechanisms exist for hollow-tube lattice structures: fracture of the tube wall, Euler (beam) buckling of a truss member, and local (shell) buckling of the tube wall (26). We define a failure mechanism (or failure mode) here to be any event that causes a loss of structural integrity of the nanolattice. Different combinations of these mechanisms can occur during

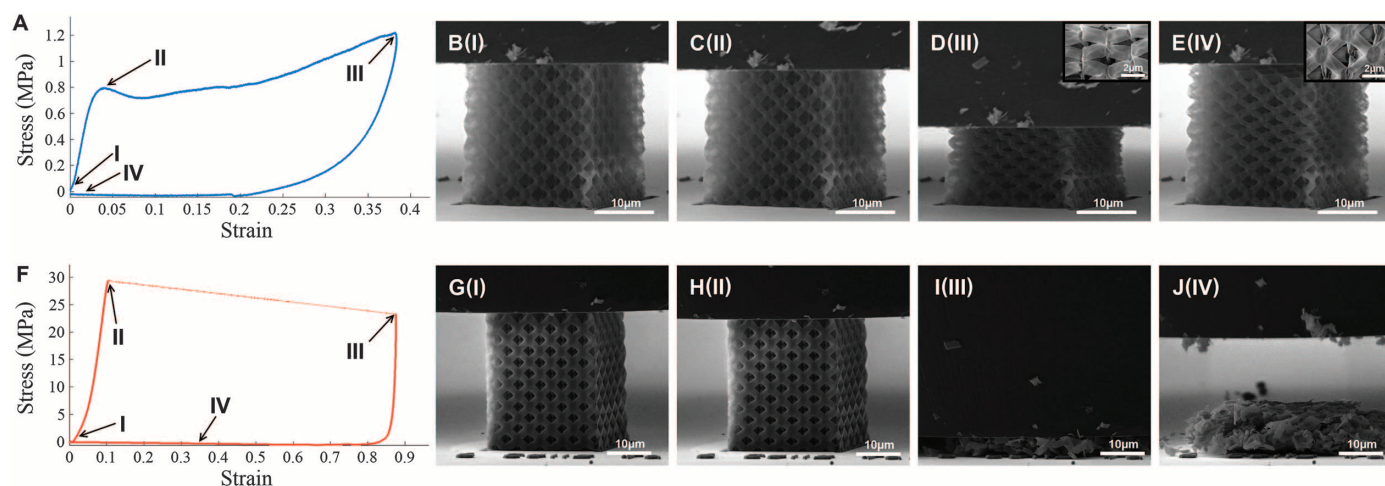


Fig. 2. Compression experiments on thick- and thin-walled nanolattices. (A to E) Mechanical data and still frames from the compression test on a thin-walled ($L = 5 \mu\text{m}$, $a = 650 \text{ nm}$, $t = 10 \text{ nm}$) nanolattice demonstrating the slow, ductile-like deformation, local shell buckling, and recovery of the structure after compression. (F to J) Mechanical data and still frames from the compression test on a thick-walled ($L = 5 \mu\text{m}$, $a = 790 \text{ nm}$, $t = 50 \text{ nm}$) nanolattice showing catastrophic brittle failure and no post-compression recovery.

deformation, depending on the stress state that arises in the beams during loading. Elastic deformation and potentially recoverability will occur in a structure when the stress necessary to initiate these processes is below the critical stress required for fracture. The condition for elastic deformation can be determined by calculating the transition point between two pairs of failure modes: shell buckling versus fracture, and Euler buckling versus fracture. Equating the stresses necessary to initiate each individual failure mechanism, we obtain an expression for the critical transition point between fracture and elastic failure [see (23) for the full derivation]

$$\left(\frac{t}{a}\right)_{\text{crit}} = \frac{\sigma_{\text{fs}}}{E} \sqrt{3(1-\nu^2)} \quad (1)$$

$$\left(\frac{a}{L}\right)_{\text{crit}} = \frac{3}{\pi} \sqrt{\frac{2\sigma_{\text{fs}}}{5E}} \quad (2)$$

Both of these functions depend on the constituent material properties: Young's modulus (E), fracture strength (σ_{fs}), and Poisson's ratio (ν). Equation 1 represents the critical ratio between the wall thickness (t) and the major radius (a) that is necessary to induce a transition between local buckling and fracture in the tubes. Equation 2 represents the critical ratio between the major radius (a) and length (L) of the tubes that describes a similar transition from Euler buckling to fracture.

Using mechanical property data reported for 75-nm-thick ALD alumina, $E = 164$ GPa, $\sigma_{\text{fs}} = 1.57$ to 2.56 GPa, $\nu = 0.24$ (27), and Eqs. 1 and 2, the critical thickness-to-radius ratio that induces a transition from yielding to shell buckling in the nanolattices was calculated to be between $(t/a)_{\text{crit}} \approx 0.0161$ and 0.0262 , and the critical radius-to-length ratio that denotes transition from yielding to Euler buckling was between $(a/L)_{\text{crit}} \approx 0.0591$ and 0.0755 . The property space of all nanolattices studied here, along with their t/a , a/L , and predicted failure modes, are shown in table S1. The experimentally observed deformation behavior of each sample is also noted in the table.

The radius-to-length ratios, a/L , for nanolattices studied here ranged from 0.0750 to 0.180 . All of these values are greater than or equal to $(a/L)_{\text{crit}}$ predicted by Eq. 2, which means that in an ideal structure, the beams will fracture before the Euler buckling condition is met. This prediction is consistent with our experimental results; no Euler buckling was observed in our *in situ* compression experiments (Fig. 2 and movies S1 to S3). This model is not capable of capturing local-scale stress concentrations, nor does it account for structures with a high degree of misalignment or pre-bending of the beams, which have been reported to reduce the critical load required to initiate buckling (6). The a/L values of the nanolattices are close to $(a/L)_{\text{crit}}$, suggesting that Euler buckling may occur in the samples with a large degree of misaligned or pre-bent

beams, but it is not observed experimentally to be a dominant deformation mechanism.

The thickness-to-diameter ratios, t/a , of the nanolattices ranged from 0.0059 to 0.0862 , which overlaps the range of $(t/a)_{\text{crit}}$ predicted by Eq. 1. For thick-walled structures, whose $t/a \geq 0.030 > (t/a)_{\text{crit}}$, the model predicts that failure of the beams is dominated by brittle fracture within the alumina tubes. Fractured segments of tubes are unable to carry any load, so every failure event will cause a strain burst whose magnitude depends on the amount of strain energy stored in the system before failure. These predictions are corroborated by experimental stress-strain data for the thick-walled structures (Figs. 2, I and J, and 3, E and F, and movie S3).

Failure in the thin-walled structures, whose $t/a \leq (t/a)_{\text{crit}} \leq 0.020$, is predicted to occur primarily via shell buckling, which is an elastic failure mode. This type of failure corresponds to a plateau in the stress-strain data caused by a gradual drop in load-carrying capacity of the beams (28), in contrast to the immediate drop in load-carrying capacity associated with fracture. Bending of an isolated thin-walled hollow beam often leads to shell buckling bifurcation, which can cause a jump in displacement (29). In a truss structure, the interactions and nodal support among all the beams delay the onset of bifurcation and allow the beams to gradually settle into a new mode. Shell buckling in thin-walled nanolattices is manifested as wrinkling

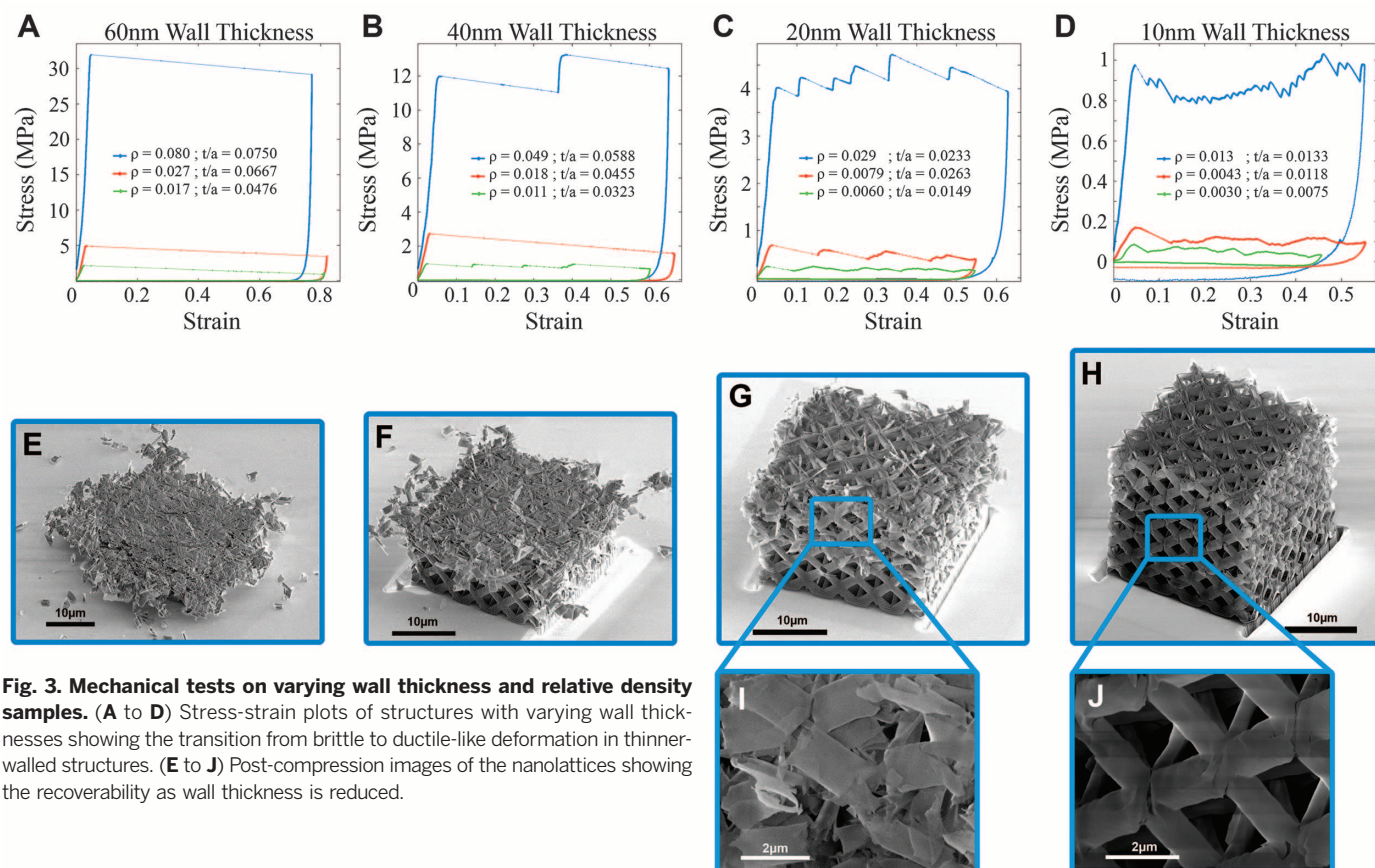


Fig. 3. Mechanical tests on varying wall thickness and relative density samples. (A to D) Stress-strain plots of structures with varying wall thicknesses showing the transition from brittle to ductile-like deformation in thinner-walled structures. (E to J) Post-compression images of the nanolattices showing the recoverability as wall thickness is reduced.

and warping of the tubes near the nodes (Figs. 2, D and E; and 3, H and J; and movie S1). The ductile-like deformation and recoverability observed in our experiments on the thin-walled nanolattices probably arise as a result of such shell buckling.

The proposed shell buckling model does not take into account the microstructural or material details, nor is it capable of predicting the deformation of structures in the transition regime of $0.020 \leq t/a \leq 0.030$. It is helpful in qualitatively explaining deformation in this regime, where nanolattices experience a complex stress state with compressive, tensile, and shear components. Fracture occurs primarily under tension, and shear and buckling occur only in compression, which means that the stress state within the beams can simultaneously satisfy fracture and buckling conditions. This is observed experimentally as a mixing of fracture and buckling failure modes, along with suppressed strain burst behavior and some recoverability (Fig. 3, G and I, and movie S2).

Elastic recovery has been studied previously in metallic and polymer lattices, and models have been proposed for their recoverability (21, 30–32). None of these works account for the observed ductile-like behavior of the ceramic nanolattices, and elastically deformable structures composed of intrinsically brittle materials such as ceramics are virtually unexplored. We postulate that reducing the t/a ratio to below $(t/a)_{\text{crit}}$ derived in

Eq. 1 enables failure via shell buckling, an elastic failure mode that causes minimal damage to the beams and nodes and allows the structure to recover. The transition to elastic failure is a necessary condition to prevent initial yielding or fracture of the constituent material but not a sufficient condition to ensure recovery of the structure. Figure 2D shows that during shell buckling, the global deformation is accompanied by localized wrinkling and warping of the tube walls. This results in confined regions of high stress that can subsequently lead to localized fracture (Figs. 2E and 3J). The propagation of these localized microcracks depends on the overall stress landscape and flaw distribution. If a crack extends into a region of high tensile stresses, or if numerous flaws reside near a crack tip, it is likely to propagate through the node and can potentially result in fracture of the tube. If an existing crack extends into a region of compressive stress, or if the stress field is insufficient to continue the crack extension, its propagation will be suppressed so that the tubes may never fully fracture. In this mechanism, a sufficient number of nodal connections remain intact to enable the structure to recover nearly fully to its original shape. The applied compressive load reduces the local tensile stresses within the tube walls that are generated by bending of the beams, which generates a compressive stress state at the nodes that can impede the propagation of a crack. As the t/a is reduced, shell buckling will commence at a lower applied

load (Eq. 1), which lowers the probability of initiating and/or propagating an existing crack. The wall thicknesses of alumina are on the order of tens of nanometers, a length scale that has been shown to exhibit enhanced strengths and damage tolerance caused by a statistically lower probability of finding a weak defect (7). These are some of the phenomena that collectively give rise to recoverability of the alumina nanolattices (Figs. 2E and 3H and Figs. S3 and S4).

We discovered that the strength and Young's modulus of all our octet-truss nanolattices follow a power law scaling with relative density as $\sigma_y \sim \bar{\rho}^{1.76}$ and $E \sim \bar{\rho}^{1.61}$ (Fig. 4, A and B). This scaling outperforms traditional lightweight and ultralight bending-dominated structural materials, whose properties scale as $E \sim \bar{\rho}^2$ or $E \sim \bar{\rho}^3$ (21), but does not follow the analytic prediction for an ideal stretching-dominated structure, $\sigma_{ys} \sim \bar{\rho}$ and $E \sim \bar{\rho}$ (20). Such a deviation from the analytic prediction can be explained, in part, by factors such as the ellipticity of the tubes, structural imperfections, and non-idealities of the experimental setup. We attribute this deviation primarily to the hollowness of the tubes, which affects the structural integrity of the nodes, where the highest stress concentrations will occur (30, 31).

The strength and deformation of an ideal, monolithic, stretching-dominated cellular solid is governed by stretching of the beams, with the nodes acting as rigid pin-jointed elements that perfectly transfer load between truss members

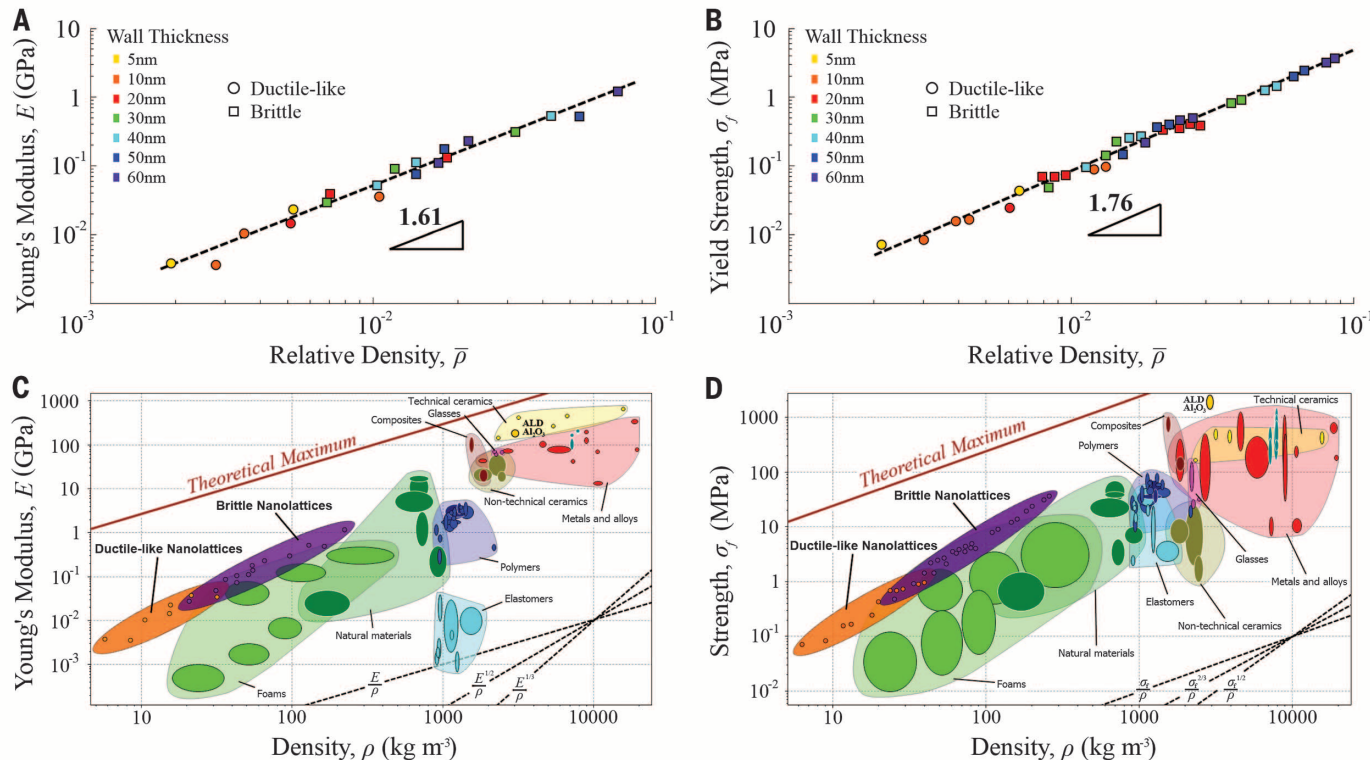


Fig. 4. Strength and stiffness versus density of alumina nanolattices. (A and B) Stiffness and strength plotted against relative density for all tested samples. Data clearly obey a power law, with little deviation across wall thicknesses and failure modes. (C and D) Material property plots (Materials Property CES Selector software by Granta Design) of the experimental stiffness and strength data against density for existing materials, showing that the materials created in this work reach a new niche in the high-strength and -stiffness lightweight material parameter space.

(20). In a hollow lattice, the nodes are constrained only by the shell walls, which has a detrimental effect on strength and stiffness because load transfer at the nodes occurs via shell wall bending. This, together with the sharp angles between the tubes, leads to an uneven distribution of stress and induces large stress concentrations in the vicinity of the nodes (Fig. 1, B and E). Bending of the tubes also causes large deflections and additional ovalization at the nodes, which further increases the compliance and stress concentrations. In situ experiments and postcompression analysis revealed that most of the deformation is localized to the nodes (Figs. 2, D and E, and 3J), which implies that improving nodal strength is a critical factor in enhancing the scaling of strength and stiffness with density.

We demonstrated the creation of ultralight hollow ceramic nanolattices that absorb energy, recover after significant compression, and reach an untapped strength and stiffness material property space. This is achieved using high-strength ALD alumina engineered into a thin-walled nanolattice that is capable of deforming elastically via shell buckling. The ultralight ceramic nanolattices represent the concept of materials by design, where it is possible to transform a strong and dense brittle ceramic into a strong, ultralight, energy-absorbing, and recoverable metamaterial. These results serve to emphasize the critical connection between material microstructure, hierarchical architecture, and mechanical properties at relevant length scales.

REFERENCES AND NOTES

1. D. Jang, L. R. Meza, F. Greer, J. R. Greer, *Nat. Mater.* **12**, 893–898 (2013).
2. J. R. Greer, J. T. M. De Hosson, *Prog. Mater. Sci.* **56**, 654–724 (2011).
3. X. W. Gu, Z. Wu, Y.-W. Zhang, D. J. Srolovitz, J. R. Greer, *Nano Lett.* **13**, 5703–5709 (2013).
4. D. Z. Chen *et al.*, *Nano Lett.* **13**, 4462–4468 (2013).
5. J. Rys *et al.*, *Adv. Eng. Mater.* **16**, 889–896 (2014).
6. L. R. Meza, J. R. Greer, *J. Mater. Sci.* **49**, 2496–2508 (2014).
7. X. Zheng *et al.*, *Science* **344**, 1373–1377 (2014).
8. J. Bauer, S. Hengsbach, I. Tesari, R. Schwaiger, O. Kraft, *Proc. Natl. Acad. Sci. U.S.A.* **111**, 2453–2458 (2014).
9. A. G. Evans, *J. Am. Ceram. Soc.* **73**, 187–206 (1990).
10. I.-W. Chen, L. A. Xue, *J. Am. Ceram. Soc.* **73**, 2585–2609 (1990).
11. P. F. Becher, *J. Am. Ceram. Soc.* **74**, 255–269 (1991).
12. D. C. Hofmann *et al.*, *Nature* **451**, 1085–1089 (2008).
13. E. Munch *et al.*, *Science* **322**, 1516–1520 (2008).
14. J. C. Weaver *et al.*, *J. Struct. Biol.* **158**, 93–106 (2007).
15. C. E. Hamm *et al.*, *Nature* **421**, 841–843 (2003).
16. M. A. Meyers, J. McKittrick, P.-Y. Chen, *Science* **339**, 773–779 (2013).
17. L. J. Gibson, M. F. Ashby, *Cellular Solids: Structure and Properties* (Cambridge Univ. Press, Cambridge, ed. 2, 1999).
18. V. S. Deshpande, M. F. Ashby, N. A. Fleck, *Acta Mater.* **49**, 1035–1040 (2001).
19. S. Pellegrino, C. R. Calladine, *Int. J. Solids Struct.* **22**, 409–428 (1986).
20. V. S. Deshpande, N. A. Fleck, M. F. Ashby, *J. Mech. Phys. Solids* **49**, 1747–1769 (2001).
21. T. A. Schaedler *et al.*, *Science* **334**, 962–965 (2011).
22. L. C. Montemayor, L. R. Meza, J. R. Greer, *Adv. Eng. Mater.* **16**, 184–189 (2014).
23. See the supplementary materials.
24. M. D. Groner, F. H. Fabreguette, J. W. Elam, S. M. George, *Chem. Mater.* **16**, 639–645 (2004).
25. Y. K. Akimov, *Instrum. Exp. Tech.* **46**, 287–299 (2003).
26. L. Valdevit, A. J. Jacobsen, J. R. Greer, W. B. Carter, *J. Am. Ceram. Soc.* **94**, s15–s34 (2011).
27. M. Berdova *et al.*, *Acta Mater.* **66**, 370–377 (2014).
28. H. G. Allen, P. S. Bulson, *Background to Buckling* (McGraw-Hill, Berkshire, UK, 1980).
29. G. Ju, S. Kyriakides, *Int. J. Solids Struct.* **29**, 1143–1171 (1992).
30. A. Torrents, T. A. Schaedler, A. J. Jacobsen, W. B. Carter, L. Valdevit, *Acta Mater.* **60**, 3511–3523 (2012).
31. L. Valdevit, S. W. Godfrey, T. Schaedler, A. J. Jacobsen, W. B. Carter, *J. Mater. Res.* **28**, 2461–2473 (2013).
32. K. J. Maloney *et al.*, *APL Mater.* **1**, 022106 (2013).

ACKNOWLEDGMENTS

The authors gratefully acknowledge the financial support from the Defense Advanced Research Projects Agency under the Materials with Controlled Microstructure and Architecture program managed by J. Goldwasser (contract no. W91CRB-10-0305) and to the Institute for Collaborative Biotechnologies through grant W911NF-09-0001 from the U.S. Army Research Office. The content of the information

does not necessarily reflect the position or the policy of the government, and no official endorsement should be inferred. The authors are grateful to the Kavli Nanoscience Institute at Caltech for the availability of critical cleanroom facilities, and to R. Lontas and C. Garland for TEM assistance. Part of this work was carried out in the Lewis Group facilities at Caltech.

SUPPLEMENTARY MATERIALS

www.sciencemag.org/content/345/6202/1322/suppl/DC1

Materials and Methods

Figs. S1 to S6

Table S1

Reference (33)

Movies S1 to S3

12 May 2014; accepted 11 August 2014

10.1126/science.1255908

WATER SPLITTING

Decoupled catalytic hydrogen evolution from a molecular metal oxide redox mediator in water splitting

Benjamin Rausch, Mark D. Symes, Greig Chisholm, Leroy Cronin*

The electrolysis of water using renewable energy inputs is being actively pursued as a route to sustainable hydrogen production. Here we introduce a recyclable redox mediator (silicotungstic acid) that enables the coupling of low-pressure production of oxygen via water oxidation to a separate, catalytic hydrogen production step outside the electrolyzer that requires no post-electrolysis energy input. This approach sidesteps the production of high-pressure gases inside the electrolytic cell (a major cause of membrane degradation) and essentially eliminates the hazardous issue of product gas crossover at the low current densities that characterize renewables-driven water-splitting devices. We demonstrated that a platinum-catalyzed system can produce pure hydrogen over 30 times faster than state-of-the-art proton exchange membrane electrolyzers at equivalent platinum loading.

Hydrogen is vital for the production of commodity chemicals such as ammonia and has great potential as a clean-burning fuel (1, 2). However, currently around 95% (~15 trillion mol year⁻¹) of the world's supply of H₂ is obtained by reforming fossil fuels (3), a process that is both unsustainable and leads to a net increase in atmospheric CO₂ levels. Of the alternative methods for H₂ production that are not linked to fossil resources, the electrolysis of water stands out as a mature, scalable technology for which the only required inputs are water and energy (in the form of electricity) (4). Hence, if the energy source is renewable, H₂ can be produced sustainably from water using electrolysis (5, 6).

Renewable energy inputs tend to be sporadic and fluctuating, and thus the systems that are developed to harness this energy and convert it to H₂ [such as proton exchange membrane electrolyzers (PEMEs) (7), solar-to-fuels systems (8), and artificial leaves (9)] must be able to deal with varying energy inputs effectively and have rapid

startup times. At the low power loads that are characteristic of renewable power sources, the rate at which H₂ and O₂ are produced may in fact be slower than the rate at which these gases permeate the membrane (10). At the very least, this will severely affect the amount of hydrogen that can be harvested from such devices (11), and in extreme cases could give rise to hazardous O₂/H₂ mixtures. The PEME is the most mature technology cited for renewables-to-hydrogen conversion, but prevention of such gas crossover at low current densities remains a challenge. PEMEs use nontrivial amounts of precious metal catalysts and so tend to operate at high current densities (1 A cm⁻² or above) and high pressure, where the cost of their components can be offset to some extent (7). However, these optimal conditions may be hard to maintain in all cases of renewables-driven electrolysis (for example, in small-scale facilities), where less-expensive and lower-power devices would therefore be beneficial. Meanwhile, the high-pressure and high-current-density conditions under which PEMEs work most effectively are also not without drawbacks: These conditions can also lead to gas crossover through the membrane, and the coexistence of H₂, O₂ and catalyst particles produces reactive oxygen species

WestCHEM, School of Chemistry, University of Glasgow, University Avenue, Glasgow G12 8QQ, UK.

*Corresponding author. E-mail: lee.cronin@glasgow.ac.uk



Strong, lightweight, and recoverable three-dimensional ceramic nanolattices

Lucas R. Meza, Satyajit Das and Julia R. Greer (September 11, 2014)

Science **345** (6202), 1322-1326. [doi: 10.1126/science.1255908]

Editor's Summary

Compressive, ductile ceramic nanolattices

Ceramics are strong and stiff, but their limited ability to stretch like putty or steels makes them unsuitable for many engineering applications. Meza *et al.* constructed ceramic nanolattices from aluminum oxide, in which the beams are designed to stretch rather than bend. A key parameter in lattice design is the ratio of the wall thickness to the beam radius. When that ratio is small enough, compressing the beams does not break them. That way, the nanolattices can be highly compressed and recover to something close to their original shape when the stress is removed.

Science, this issue p. 1322

This copy is for your personal, non-commercial use only.

- | | |
|----------------------|--|
| Article Tools | Visit the online version of this article to access the personalization and article tools:
http://science.sciencemag.org/content/345/6202/1322 |
| Permissions | Obtain information about reproducing this article:
http://www.sciencemag.org/about/permissions.dtl |

Science (print ISSN 0036-8075; online ISSN 1095-9203) is published weekly, except the last week in December, by the American Association for the Advancement of Science, 1200 New York Avenue NW, Washington, DC 20005. Copyright 2016 by the American Association for the Advancement of Science; all rights reserved. The title *Science* is a registered trademark of AAAS.